Applied Physics Letters

Understanding efficiency improvements of betavoltaic batteries based on 4H-SiC, GaN, and diamond

Cite as: Appl. Phys. Lett. **121**, 103902 (2022); https://doi.org/10.1063/5.0102995
Submitted: 14 June 2022 • Accepted: 20 August 2022 • Published Online: 08 September 2022

Renzhou Zheng, Jingbin Lu, Yu Wang, et al.

Applied Physics Letters ARTICLE scitation.org/journal/apl

Understanding efficiency improvements of betavoltaic batteries based on 4H-SiC, GaN, and diamond

Cite as: Appl. Phys. Lett. **121**, 103902 (2022); doi: 10.1063/5.0102995
Submitted: 14 June 2022 · Accepted: 20 August 2022 ·
Published Online: 8 September 2022

Renzhou Zheng,[1] Jingbin Lu,[1,a)] Yu Wang,[1] Ziyi Chen,[1] Xue Zhang,[1] Xiaoyi Li,[1] Lei Liang,[2,3,4,a)] Li Qin,[2] Yugang Zeng,[2] Yongyi Chen,[2] and Yumin Liu[5]

AFFILIATIONS

[1]College of Physics, Jilin University, Changchun 130012, China
[2]State Key Laboratory of Luminescence and Applications, Changchun Institute of Optics, Fine Mechanics and Physics, Chinese Academy of Sciences, Changchun 130033, China
[3]Center of Materials Science and Optoelectronics Engineering, University of Chinese Academy of Sciences, Beijing 100049, China
[4]Peng Cheng Laboratory, No. 2, Xingke 1st Street, Shenzhen 518000, China
[5]College of Nuclear Science and Engineering, East China University of Technology, Nanchang 330013, China

[a)]**Authors to whom correspondence should be addressed:** ljb@jlu.edu.cn and liangl@ciomp.ac.cn

ABSTRACT

Wide-bandgap semiconductors are more advantageous for betavoltaic batteries due to their high conversion efficiency and strong radiation resistance. However, there has been little comprehensive analysis of how wide-bandgap semiconductors lead to efficiency improvements. In this work, we proposed a simulation model to predict the output performance of betavoltaic batteries based on 4H-SiC, hexagonal-GaN, and diamond, in which the Monte Carlo code and COMSOL Multiphysics software were combined. The energy deposition of a ^{63}Ni source in semiconductors and the electrical characteristics of p–n junctions were investigated and compared. Our simulation results showed that the mass density and atomic number of semiconductor materials will cause the difference in energy deposition distribution, further leading to the different electron–hole pair generation rates. Then, the internal efficiency of batteries is co-determined by the energy band structure, depletion region width, built-in potential barrier, and minority carrier lifetime. The batteries based on wide-bandgap semiconductors can achieve the larger open-circuit voltage, further leading to higher efficiency. Additionally, to optimize the energy converter structure, the output parameters were calculated with a variation of doping concentrations and thicknesses of each region. Under the irradiation of a ^{63}Ni source, the diamond-based battery with a p–n junction structure has the highest internal efficiency of 31.3%, while the GaN-based battery has the lowest one (16.8%), which can be attributed to the larger carrier recombination rate.

In recent years, radioisotope micro-batteries have attracted much attention in the field of low-power devices, where micro-power sources with long service life, small scale, and high power density are urgently needed.[1,2] They typically consist of a radioactive source and a semiconductor energy converter, the radioactive source can be an x ray, gamma-ray, alpha particle, or beta particle source, and the semiconductors generally include Si, GaAs, GaP, SiC, GaN, diamond, etc.[3,4] Due to their advantages of easy shielding and small radiation damage, the betavoltaic batteries are more attractive than other types, and they can convert the decay energy into electrical energy in a similar way to solar cells. Researchers have done theoretical and experimental studies on the battery performance, and considerable efforts have been devoted to the optimization design in terms of semiconductor materials and device structures.[5,6]

Si-based betavoltaic batteries were first studied due to their mature technology and low cost.[7] However, the low conversion efficiency and poor radiation resistance limited their application space.[1,4] Theoretical studies showed that using wide-bandgap semiconductors is beneficial to improve the conversion efficiency of batteries,[8] so the focus of researchers gradually turned toward the batteries based on wide-bandgap semiconductors. As a III–V compound semiconductor, GaAs was an excellent material for space solar cells, and it was also suitable for betavoltaic batteries.[9] Unfortunately, the minority carrier diffusion lengths of GaAs are too small, this means multiple devices

need to be connected in series to improve the collection efficiency.[4] Semiconductors with wider bandgap seem to be a better option, and betavoltaic batteries based on SiC,[10,11] GaN,[12,13] and diamond[14,15] have been demonstrated. In 2020, a SiC-based p–n junction battery was fabricated.[16] Under 20 keV electron beam irradiation, the conversion efficiency was measured as 20.17%. In 2021, a GaN-based p–i–n junction battery was reported, and the conversion efficiency was 6.6% under 30 keV electron beam irradiation.[17] In 2020, a betavoltaic battery using a diamond p–n junction achieved a semiconductor conversion efficiency of 28% under 20 keV electron beam irradiation.[18] These are the highest values ever reported for betavoltaic batteries.

From these reports, the batteries based on wide-bandgap semiconductors exhibit better output performance, and the conversion efficiency increases with increasing bandgap, which is well-accepted. Prelas *et al.* defined the driving potential efficiency as the ratio of open-circuit voltage to bandgap, so as to link the transducer efficiency to bandgap.[5] Maximenko *et al.* analyzed the Shockley equation and concluded that an increase in bandgap leads the reverse saturation current density to decrease and the open-circuit voltage to increase, thereby improving the semiconductor conversion efficiency.[19] Zhao *et al.* attributed the high conversion efficiency of batteries based on wide-bandgap semiconductors to the low recombination loss, which is represented by the open-circuit voltage loss.[6] These results explained in different ways how wide-bandgap semiconductors improve the battery efficiency. However, there has been little discussion in terms of the device energy band structure and radiation-induced carrier transport, which directly determine the output performance. Therefore, it is necessary to conduct a systematic investigation to understand the energy conversion process and factors that affect conversion efficiency. This can provide a reference for the selection and evaluation of wide-bandgap semiconductors for betavoltaic batteries.

In this paper, we predicted the output performance of betavoltaic batteries based on wide-bandgap semiconductors by the Monte Carlo N-Particle Transport Code, Version 5 (MCNP5-1.51, 2009.01) and COMSOL Multiphysics software (version: 5.4, 2018.10). The energy deposition of a ^{63}Ni source and electrical characteristics of p–n junctions in 4H-SiC, hexagonal-GaN, and diamond-based batteries were investigated and compared. Then, the effect of factors on conversion efficiency, including the energy band structure, depletion region width, built-in potential barrier, and carrier generation, recombination, and collection, were systematically analyzed. Moreover, to optimize the energy converter structure, the short-circuit current density, open-circuit voltage, and maximum output power density were calculated with a variation in doping concentrations and thicknesses of each region. This work provides a perspective for understanding the efficiency improvements of betavoltaic batteries by using the wide-bandgap semiconductors.

The output power of a betavoltaic battery depends on the energy deposition of beta particles in semiconductor materials and the collection of radiation-induced electron–hole pairs in energy converters. In this study, the betavoltaic batteries are co-simulated by the Monte Carlo code and COMSOL Multiphysics software, and in order to connect these two parts, the average energy dissipated per electron–hole pair generated (E_{ehp}) is used to estimate the electron–hole pair generation rate distribution from the energy deposition distribution.[20]

The Monte Carlo code is used to simulate the energy deposition distribution of ^{63}Ni beta particles in semiconductor materials, including 4H-SiC, hexagonal-GaN, and diamond. Previous studies have shown that as the source thickness increases, the apparent power density reaches saturation due to the self-absorption effect.[21] Therefore, a rectangular ^{63}Ni source with an optimal thickness of 2 μm and a full energy spectrum are used in the simulation model (a cross-sectional area of 1×1 cm^2 and a total activity density of 100 mCi/cm^2). In order to ensure complete energy deposition, the total thickness of the semiconductor material bulk is set as 0.5 cm (a cross-sectional area of 1×1 cm^2). The number of particles simulated is 10^8, and the error is below 0.01.

The energy deposition rates in semiconductor materials vs the radiation transport depth are shown in Fig. 1(a) and also the accumulation energy deposition distributions. It is seen that the energy deposition rate decreases rapidly with increasing depth, especially in GaN due to its largest mass density. This means that the beta energy is mainly deposited near the material surface; thus, a shallow junction is more appropriate when designing the semiconductor energy converters. Figure 1(a) also shows that the accumulation energy deposition increases with depth, eventually reaching saturation. According to the definition of penetration depth that the position where 99% of the total energy is deposited,[22] the specific values are 7.5, 4.1, and 7.2 μm in 4H-SiC, GaN, and diamond, respectively. In addition, the total energy deposition power density is largest in diamond (1.53 μW/cm^2), followed by 4H-SiC (1.44 μW/cm^2) and GaN (1.27 μW/cm^2). This can

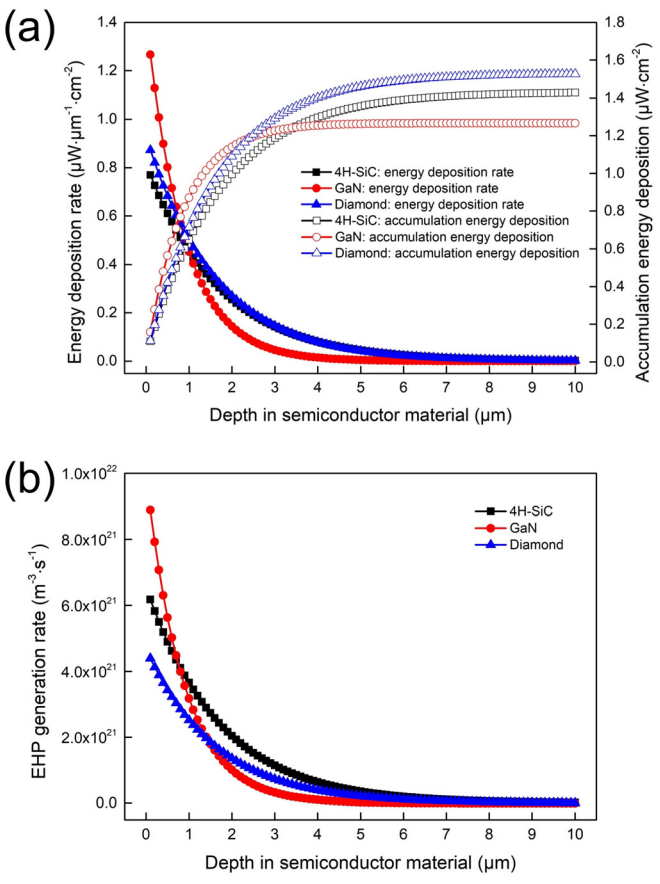

FIG. 1. (a) Energy deposition distributions of ^{63}Ni beta particles and (b) electron–hole pair (EHP) generation rate distributions in 4H-SiC, GaN, and diamond.

be explained considering the backscattering losses of beta particles. The energy backscattering coefficient depends on the atomic number of semiconductor materials, and it is 11.8% for diamond ($Z = 6$), 19.8% for 4H-SiC ($Z = 10$), and 32.5% for GaN ($Z = 19$).

Furthermore, the electron–hole pair (EHP) generation rates in semiconductor materials vs the radiation transport depth are obtained, as shown in Fig. 1(b). The EHP generation rate decreases exponentially with increasing radiation transport depth (Y), and it is expressed as

$$G(Y) = \frac{E(Y)}{E_{\text{ehp}}} = G_0 \exp(-\alpha Y), \tag{1}$$

where $E(Y)$ is the energy deposition rate from Fig. 1(a), E_{ehp} is the average energy dissipated per electron–hole pair generated, and G_0 and α are the exponential fitting parameters, as listed in Table I. It should be noted that the predicted values for E_{ehp} from the Klein formula are different than the measured values especially for wider bandgap semiconductors. Therefore, the measured values reported in the literature are used,[5] which agree with the predicted values from the Bertuccio–Maiocchi–Barnett (BMB) relationship.[23]

COMSOL Multiphysics software is used to simulate the electrical characteristics of energy converters, and the p–n junctions based on 4H-SiC, hexagonal-GaN, and diamond are modeled. To obtain a fast computation time, the cross-sectional area of a device is set as 1×1 μm^2, and the total thickness is set as 30 μm. The thicknesses of the p-region and n-region are variables, denoted as $H_{\text{p-region}}$ and $H_{\text{n-region}}$, respectively. The acceptor concentration of the p-region and the donor concentration of the n-region are denoted as N_a and N_d, respectively. In the following simulations, these structure parameters will be optimized to maximize the battery output power.

To simulate the transport and collection of radiation-induced carriers, the Poisson and carrier continuity equations are solved as[24–26]

$$\nabla^2 V = -\frac{\rho}{\epsilon_0 \epsilon_r}, \tag{2}$$

$$-\frac{1}{q}\nabla j_n = G - R_n, \tag{3}$$

$$\frac{1}{q}\nabla j_p = G - R_p, \tag{4}$$

where ρ is the charge density, ϵ_r is the relative permittivity of material, V is the electrostatic potential, ϵ_0 is the vacuum permittivity, R_n (R_p) is the electron (hole) recombination rate, G is the electron–hole pair generation rate, and q is the electron charge. j_n (j_p) is the electron (hole) current density, and it is expressed as

$$j_n = -\frac{\mu_n kT}{q}\nabla n + \mu_n n \nabla V, \tag{5}$$

TABLE I. The E_{ehp} of semiconductor materials and the fitting parameters of the electron–hole pair generation rate.

Materials	E_{ehp} (eV)[5]	G_0 ($\times 10^{21}$ m$^{-3} \cdot$ s^{-1})	α (μm^{-1})
4H-SiC	7.78	6.5443	0.581 59
GaN	8.9	9.9560	1.142 19
Diamond	12.4	4.6726	0.615 91

$$j_p = -\frac{\mu_p kT}{q}\nabla p - \mu_p p \nabla V, \tag{6}$$

where μ_n (μ_p) is the electron (hole) mobility, n (p) is the electron (hole) concentration, T is the absolute temperature, and k is Boltzmann's constant.

In addition, various physical models are employed to define additional components. For example, the background concentration and the main p and n regions of the device are defined by the analytic doping model. The changes in minority carrier mobility with doping concentration are calculated by the low-field mobility model.[27–29] The trap-assisted recombination is defined by the Shockley–Read–Hall (SRH) recombination model. The electron–hole pair generation is defined according to the Monte Carlo simulation results (Figure 1 and Table I, the p-region is the incident position of beta particles). In the COMSOL calculations, the tolerance is less than 10^{-6}.

Figure 2(a) shows the energy diagram of the batteries based on 4H-SiC, GaN, and diamond at thermodynamic equilibrium. In the

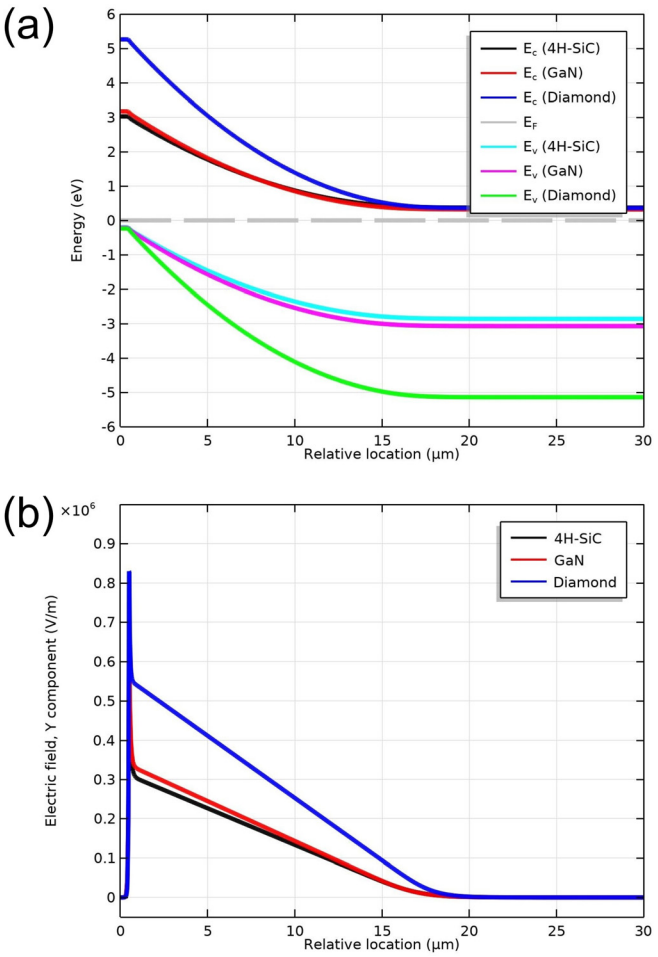

FIG. 2. (a) Energy diagram and (b) electric field Y-component distribution of the batteries based on 4H-SiC, GaN, and diamond at thermodynamic equilibrium. The $H_{\text{p-region}}$, $H_{\text{n-region}}$, N_a, and N_d values are 0.5 μm, 29.5 μm, 1×10^{16}cm^{-3}, and 1×10^{13}cm^{-3}, respectively.

space charge region, the conduction band (E_c) and the valence band (E_v) are bent, and an energy potential barrier (built-in potential barrier) is formed. The diamond-based battery has the highest energy potential barrier of 4.91 eV, followed by the GaN-based battery (2.86 eV) and 4H-SiC-based battery (2.66 eV). This observation can be explained by the wider bandgap bringing the lower intrinsic carrier concentration, and then the higher energy potential barrier can be obtained, which is beneficial to achieve a larger open-circuit voltage.

In the p–n junction batteries, the transport and collection of radiation-induced carriers are affected by the electric field Y-component (normal to the junction plane) distribution. As shown in Fig. 2(b), the electric field is mainly distributed in the depletion region (the positive direction is the n-region pointing to the p-region), where the radiation-induced electron–hole pairs can be separated. The variation in the electric field intensity with position agrees with the band bending in Fig. 2(a). In addition, the depletion region widths are 16.9, 16.8, and 17.6 μm for 4H-SiC-, GaN-, and diamond-based batteries, respectively, indicating that the electron–hole pairs can be collected effectively.

In order to evaluate the battery performance, the current density–voltage (J–V) characteristics are extracted by sweeping the forward voltage across the device. The current density–voltage (J–V) and power density–voltage (P–V) characteristics of the batteries based on 4H-SiC, GaN, and diamond are shown in Fig. 3(a). It is observed that the 4H-SiC-based battery has the largest short-circuit current density (J_{sc}) of 156 nA/cm^2, which can be attributed to the smallest E_{ehp} (7.78 eV) bringing the most electron–hole pairs generated in the energy converter. In contrast, the total energy deposition power density is largest in diamond (1.53 μW/cm^2), but the E_{ehp} of 12.4 eV suggests a rather low electron–hole pair generation rate. In terms of the open-circuit voltage (V_{oc}), the highest built-in potential barrier (4.91 V) of the diamond-based battery contributes to the largest V_{oc} of 4.34 V, further leading to the largest maximum output power density (P_m) of 425 nW/cm^2.

In addition, the carrier recombination has significant effects on the battery performance, which depends on the minority carrier lifetime. In our simulation model, the lifetime values (τ_n and τ_p) are based on the current technology reported in the literature.[27,28,30] The Shockley–Read–Hall (SRH) recombination rates across the batteries based on 4H-SiC, GaN, and diamond are shown in Fig. 3(b). When the doping concentrations are $N_a = 1 \times 10^{16}$ and $N_d = 1 \times 10^{13}$cm^{-3}, the minority carrier lifetimes (τ_n and τ_p) in GaN are less than 1 ns, while they are more than 100 ns in 4H-SiC and diamond. The relatively small carrier lifetimes result in the larger recombination rate, especially around the p-region, where the beta particles are incident and the EHP generation rate is higher. This is why the GaN-based battery has the smallest V_{oc} and P_m in Fig. 3(a).

We define the battery internal efficiency (η_i) by the following equation, which represents the ability to convert absorbed energy into electrical energy:

$$\eta_i = \frac{P_m}{P_{in}}, \tag{7}$$

where P_{in} is the total energy deposition power density entering the semiconductor material from the radioactive beta source. Then, the

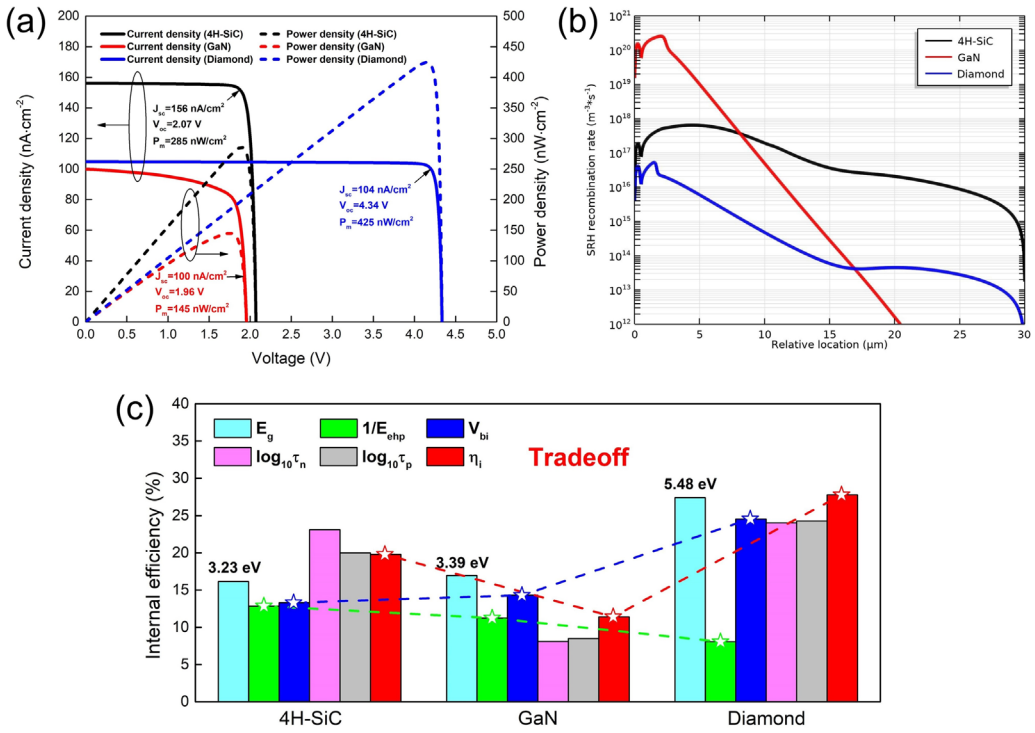

FIG. 3. (a) J–V and P–V characteristics. (b) Shockley–Read–Hall (SRH) recombination rates. (c) Internal efficiency (η_i) difference of the batteries based on 4H-SiC, GaN, and diamond, and changes in E_g, E_{ehp}, V_{bi}, τ_n, and τ_p. The $H_{p-region}$, $H_{n-region}$, N_a, and N_d values are 0.5 μm, 29.5 μm, 1 $\times 10^{16}$cm^{-3}, and 1 $\times 10^{13}$cm^{-3}, respectively.

internal efficiency difference of the batteries based on 4H-SiC, GaN, and diamond is shown in Fig. 3(c). The changes in bandgap (E_g), average energy dissipated per electron–hole pair generated (E_{ehp}), built-in potential barrier (V_{bi}), minority electron lifetime (τ_n), and minority hole lifetime (τ_p) are also plotted. For comparison, the reciprocal or logarithmic values of some parameters are taken, and the effects of $1/E_{ehp}$, V_{bi}, $\log_{10}\tau_n$, and $\log_{10}\tau_p$ on η_i are shown. (A large value indicates a large contribution.) Since the dimensions of each parameter are different, the height of bar chart only shows the relative sizes for different semiconductor materials. It is clear to see that from the 4H-SiC-based battery to diamond-based battery, the contribution of $1/E_{ehp}$ to η_i decreases, correspondingly the electron–hole pair generation rate decreases. Conversely, the contribution of V_{bi} increases, which is beneficial to achieve a larger V_{oc}. It can also be seen that for the GaN-based battery, the τ_n and τ_p contribute very little, further leading to a significant decrease in η_i. In conclusion, the internal efficiency of betavoltaic batteries depends on the trade-off among various factors, and ideally, the batteries based on wide-bandgap semiconductors can achieve a higher efficiency because of the larger open-circuit voltage. However, practically, considering the current technology, the minority carrier lifetimes of some wide-bandgap semiconductors are relatively small.[31] This means smaller minority carrier diffusion lengths and a larger recombination rate, which are disadvantageous to the efficiency improvements. Therefore, the selection and evaluation of wide-bandgap semiconductors should be based on these simulation results taking into account the realistic parameters.

Generally, the battery performance is also affected by the energy converter structure. Due to the different semiconductor properties (as mentioned above), the effects of doping concentrations and thicknesses of each region on the output parameters of batteries based on different semiconductors are also different. Figure 4 shows the variations in the short-circuit current density (J_{sc}), open-circuit voltage (V_{oc}), and maximum output power density (P_m) depending on the N_a and N_d for the batteries based on 4H-SiC, GaN, and diamond. It is seen that the J_{sc} decreases with increasing N_a, which can be attributed to the decrease in the depletion region width. To validate this, Figure 5 shows the energy diagram of the GaN-based battery as an example. As N_a increases, the depletion region extends more in the n-region, where the EHP generation rate is lower, further leading to the decrease in J_{sc}. In addition, the J_{sc} also decreases with increasing N_d, but the GaN-based battery shows a trend of increasing first and then decreasing. This is related to the combined effect of the depletion region extending more in the p-region and depletion region width decreasing. Next, Figs. 4(b), 4(e), and 4(h) show that the V_{oc} is insensitive to N_a, and it increases with increasing N_d, which can be explained by the higher built-in potential barrier (as shown in Fig. 5). Ultimately, as shown in

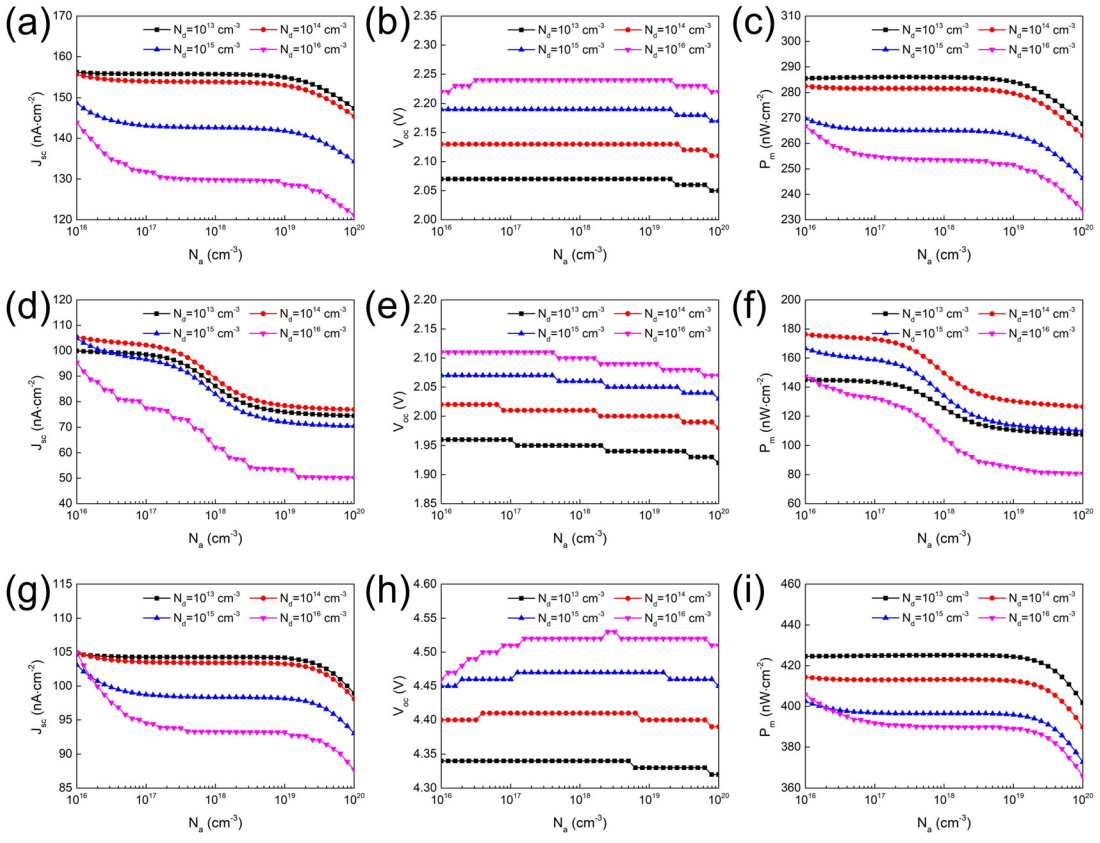

FIG. 4. Variations of (a) J_{sc}, (b) V_{oc}, and (c) P_m dependent on the N_a and N_d for the 4H-SiC-based battery. (d) J_{sc}, (e) V_{oc}, and (f) P_m for the GaN-based battery. (g) J_{sc}, (h) V_{oc}, and (i) P_m for the diamond-based battery. The $H_{p\text{-region}}$ and $H_{n\text{-region}}$ values are 0.5 and 29.5 μm, respectively.

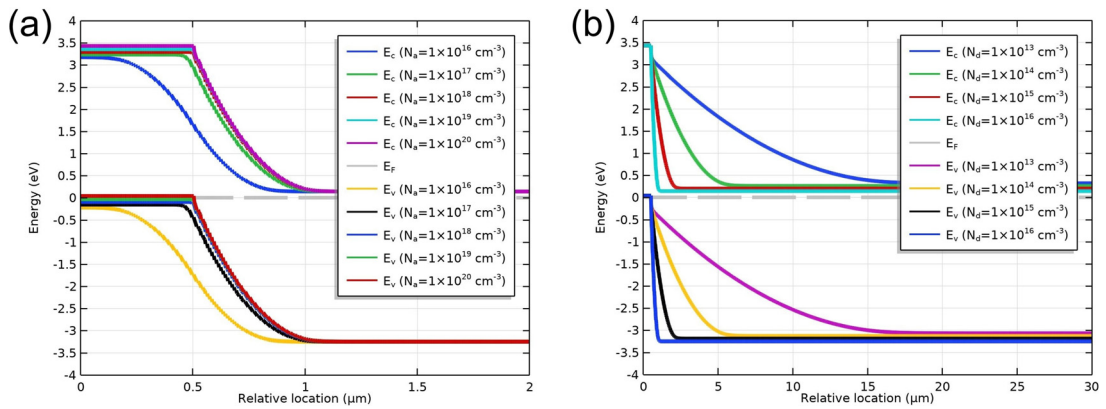

FIG. 5. Energy diagram of the GaN-based battery at thermodynamic equilibrium. (a) When N_a is changed, N_d is fixed as 1 $\times 10^{16}$cm^{-3}. (b) When N_d is changed, N_a is fixed as 1 $\times 10^{20}$cm^{-3}. The $H_{\text{p-region}}$ and $H_{\text{n-region}}$ values are 0.5 and 29.5 μm, respectively.

Figs. 4(c), 4(f), and 4(i), the P_m decreases with increasing N_a, and it also decreases with increasing N_d, except for the GaN-based battery, which increases first and then decreases.

After determining the optimal values of doping concentrations (N_a and N_d), the variations of J_{sc}, V_{oc}, and P_m depending on the $H_{\text{p-region}}$ for the batteries based on 4H-SiC, GaN, and diamond are shown in Figs. 6(a)–6(c). Correspondingly, the electric field Y-component distribution of the batteries at thermodynamic equilibrium is shown in Fig. 6(d). When $H_{\text{p-region}}$ increases, the depletion region gets away from the energy converter surface, where the EHP generation rate is higher. As a result, the J_{sc} decreases, especially for the GaN-based battery, in which the EHP distribution range and depletion region width are smaller. In addition, the rather large V_{oc} makes the P_m of diamond-based battery always the largest. To be specific, as $H_{\text{p-region}}$ increases from 0.1 to 5 μm, the P_m of diamond-based battery decreases from 479 to 151 nW/cm^2, while the P_m of GaN-based battery decreases from 214 nW/cm^2 to less than 10

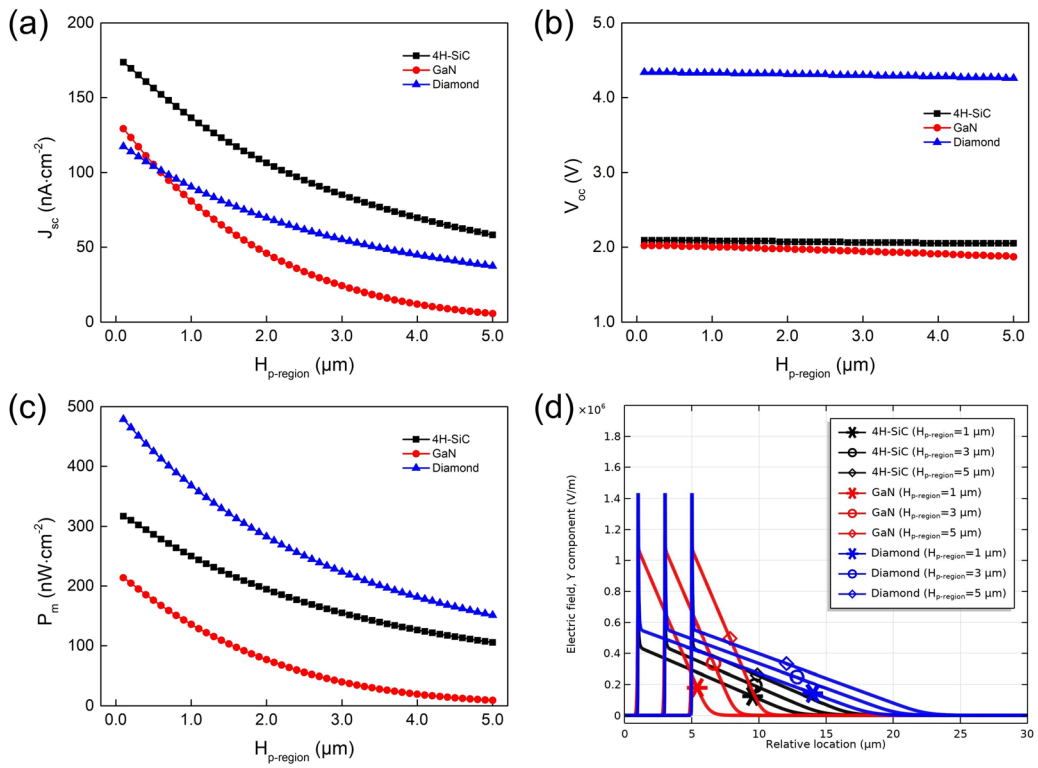

FIG. 6. Variations of (a) J_{sc}, (b) V_{oc}, and (c) P_m dependent on the $H_{\text{p-region}}$ for the batteries based on 4H-SiC, GaN, and diamond. (d) Electric field Y-component distribution of the batteries at thermodynamic equilibrium. When $H_{\text{p-region}}$ is changed, $H_{\text{n-region}} = 30$ μm-$H_{\text{p-region}}$. The N_a and N_d values are optimized.

TABLE II. Performance comparison of the batteries based on 4H-SiC, GaN, and diamond.

Semiconductors	$H_{p-region}$ (μm)	$H_{n-region}$ (μm)	N_a (cm^{-3})	N_d (cm^{-3})	J_{sc} (nA/cm^2)	V_{oc} (V)	P_m (nW/cm^2)	η_i (%)
4H-SiC	0.1	29.9	1×10^{16}	2×10^{13}	174	2.09	317	22.0
GaN	0.1	29.9	1×10^{16}	1×10^{14}	129	2.02	214	16.8
Diamond	0.1	29.9	1×10^{17}	1×10^{13}	118	4.34	479	31.3

nW/cm^2. These results suggest that a shallow junction is more appropriate for a betavoltaic battery with a p–n junction structure. Finally, the performance comparison of the batteries based on 4H-SiC, GaN, and diamond is listed in Table II. These results agree with experimental values reported in the literature, where the diamond-based p–n junction battery achieved a conversion efficiency of 28%.[18]

In summary, the betavoltaic batteries based on wide-bandgap semiconductors, including 4H-SiC, hexagonal-GaN, and diamond, were modeled, and the output performance and efficiency improvement were evaluated. First, the Monte Carlo code was used to simulate the energy deposition of ^{63}Ni beta particles in energy conversion materials. The results showed that the energy deposition distribution depends on the mass density and atomic number of the target material for the same radioactive source. The total energy deposition power density of 1.53 $\mu W/cm^2$ is largest in diamond. Second, COMSOL Multiphysics software was used to simulate the electrical characteristics of p–n junctions and predict the battery performance. The internal efficiency of betavoltaic batteries depends on the trade-off among various factors, and it is co-determined by the bandgap, average energy dissipated per electron–hole pair generated, depletion region width, built-in potential barrier, and minority carrier lifetime. The calculations showed that the batteries based on wide-bandgap semiconductors can achieve a larger open-circuit voltage and, hence, higher efficiency. However, for some semiconductors with small minority carrier lifetimes limited by current technology, the large recombination rate can lead to a significant decrease in efficiency. In addition, the effects of an energy converter structure on battery output parameters were analyzed. Low doping concentrations are beneficial to enlarge the depletion region width, and then a large short-circuit current density can be obtained. Whereas high doping concentrations lead to a high built-in potential barrier, further enhancing the open-circuit voltage. Finally, the diamond-based battery can achieve the highest internal efficiency of 31.3%. The related J_{sc}, V_{oc}, and P_m are 118 nA/cm^2, 4.34 V, and 479 nW/cm^2, respectively. These results can provide theoretical references and valuable guidance for the optimization design and experimental fabrication of high-performance betavoltaic batteries. The selection and evaluation of wide-bandgap semiconductors should be based on these simulations considering the realistic parameters.

This work was supported by the National Natural Science Foundation of China (Nos. 11075064 and U1867210) and the National Major Scientific Instruments and Equipment Development Projects (No. 2012YQ240121).

AUTHOR DECLARATIONS

Conflict of Interest

The authors have no conflicts to disclose.

Author Contributions

Renzhou Zheng: Conceptualization (equal); Data curation (equal); Formal analysis (equal); Investigation (equal); Methodology (equal); Writing – original draft (equal); Writing – review & editing (equal). **Yongyi Chen:** Conceptualization (equal); Software (equal). **Yumin Liu:** Conceptualization (equal). **Jing-Bin Lu:** Conceptualization (equal); Investigation (equal); Methodology (equal); Project administration (equal); Writing – review & editing (equal). **Yu Wang:** Conceptualization (equal); Formal analysis (equal); Investigation (equal); Methodology (equal). **Ziyi Chen:** Conceptualization (equal); Investigation (equal); Methodology (equal). **Xue Zhang:** Conceptualization (equal); Investigation (equal); Methodology (equal). **XiaoYi Li:** Conceptualization (equal); Investigation (equal). **Lei Liang:** Conceptualization (equal); Software (equal). **Li Qin:** Conceptualization (equal); Software (equal). **Yugang Zeng:** Conceptualization (equal); Software (equal).

DATA AVAILABILITY

The data that support the findings of this study are available from the corresponding authors upon reasonable request.

REFERENCES

[1]L. C. Olsen, P. Cabauy, and B. J. Elkind, "Betavoltaic power sources," Phys. Today **65**(12), 35–38 (2012).
[2]M. A. Prelas, C. L. Weaver, M. L. Watermann, E. D. Lukosi, R. J. Schott, and D. A. Wisniewski, "A review of nuclear batteries," Prog. Nucl. Energy **75**, 117–148 (2014).
[3]G. Lioliou, A. B. Krysa, and A. M. Barnett, "Wide bandgap semiconductor conversion devices for radioisotope microbatteries," Mater. Sci. Semicond. Process. **142**, 106533 (2022).
[4]M. G. Spencer and T. Alam, "High power direct energy conversion by nuclear batteries," Appl. Phys. Rev. **6**, 031305 (2019).
[5]M. A. Prelas, M. Boraas, F. D. Aguilar, J. D. Seelig, M. T. Tchouaso, and D. Wisniewski, *Nuclear Batteries and Radioisotopes, Lecture Notes in Energy* (Springer Press, 2016), Vol. 56.
[6]C. Zhao, F. Y. Liao, K. Z. Liu, and Y. Y. Zhao, "Breaking the myth: Wide-bandgap semiconductors not always the best for betavoltaic batteries," Appl. Phys. Lett. **119**, 153904 (2021).
[7]P. Rappaport, "The electron-voltaic effect in p–n junctions induced by beta-particle bombardment," Phys. Rev. **93**(1), 246 (1954).
[8]L. C. Olsen, "Betavoltaic energy conversion," Energy Convers. **13**(4), 117–127 (1973).
[9]K. E. Bower, Y. A. Barbanel, Y. G. Shreter, and G. W. Bohnert, *Polymers, Phosphors and Voltaics for Radioisotope Microbatteries* (CRC Press, Boca Raton, FL, 2002).
[10]M. V. S. Chandrashekhar, C. I. Thomas, H. Li, M. G. Spencer, and A. Lal, "Demonstration of a 4H SiC betavoltaic cell," Appl. Phys. Lett. **88**, 033506 (2006).
[11]D.-Y. Qiao, X.-J. Chen, Y. Ren, and W.-Z. Yuan, "A micro nuclear battery based on SiC Schottky barrier diode," J. Microelectromech. Syst. **20**(3), 685–690 (2011).

[12]Z.-J. Cheng, H.-S. San, X.-Y. Chen, B. Liu, and Z.-H. Feng, "Demonstration of a high open-circuit voltage GaN betavoltaic microbattery," Chin. Phys. Lett. **28**(7), 078401 (2011).
[13]M. Lu, G-g Zhang, K. Fu, G-h Yu, D. Su, and J-f Hu, "Gallium nitride Schottky betavoltaic nuclear batteries," Energy Convers. Manage. **52**(4), 1955–1958 (2011).
[14]V. Bormashov, S. Troschiev, A. Volkov, S. Tarelkin, E. Korostylev, A. Golovanov, M. Kuznetsov, D. Teteruk, N. Kornilov, S. Terentiev, S. Buga, and V. Blank, "Development of nuclear microbattery prototype based on Schottky barrier diamond diodes," Phys. Status Solidi A **212**(11), 2539–2547 (2015).
[15]Y.-M. Liu, J.-B. Lu, X.-Y. Li, X. Xu, R. He, R.-Z. Zheng, and G.-D. Wei, "Theoretical prediction of diamond betavoltaic batteries performance using ^{63}Ni," Chin. Phys. Lett. **35**, 072301 (2018).
[16]C. Zhao, A. Liu, S. Bai, and Y. Y. Zhao, "Understanding efficiency differences of betavoltaic batteries measured by electron gun mimicked source and radioactive β source," Appl. Phys. Lett. **117**, 193901 (2020).
[17]T. Heuser, M. Braun, P. Mclntyre, and D. G. Senesky, "Electron beam irradiation of gallium nitride-on-silicon betavoltaics fabricated with a triple mesa etch," J. Appl. Phys. **130**, 174503 (2021).
[18]T. Shimaoka, H. Umezawa, K. Ichikawa, J. Pernot, and S. Koizumi, "Ultrahigh conversion efficiency of betavoltaic cell using diamond pn junction," Appl. Phys. Lett. **117**, 103902 (2020).
[19]S. Maximenko, J. Moore, C. Affouda, and P. Jenkins, "Optimal semiconductors for ^{3}H and ^{63}Ni betavoltaics," Sci. Rep. **9**, 10892 (2019).
[20]C. A. Klein, "Bandgap dependence and related features of radiation ionization energies in semiconductors," J. Appl. Phys. **39**, 2029–2038 (1968).
[21]Y.-P. Liu, X.-B. Tang, Z.-H. Xu, L. Hong, H. Wang, M. Liu, and D. Chen, "Influences of planar source thickness on betavoltaics with different semiconductors," J. Radioanal. Nucl. Chem. **304**, 517–525 (2015).
[22]T. R. Alam, M. A. Pierson, and M. A. Prelas, "Beta particle transport and its impact on betavoltaic battery modeling," Appl. Radiat. Isot. **130**, 80 (2017).
[23]G. Lioliou and A. M. Barnett, "Electron–hole pair creation and conversion efficiency in radioisotope microbatteries," Appl. Radiat. Isot. **180**, 110042 (2022).
[24]X. Li, N. P. Hylton, V. Giannini, K.-H. Lee, N. J. Ekins-Daukes, and S. A. Maier, "Multi-dimensional modeling of solar cells with electromagnetic and carrier transport calculations," Prog. Photovoltaics: Res. Appl. **21**, 109–120 (2013).
[25]N. Bednar, N. Severino, and N. Adamovic, "Optical simulation of light management in CIGS thin-film solar cells using finite element method," Appl. Sci. **5**, 1735–1744 (2015).
[26]D. A. Neamen, *Semiconductor Physics and Devices: Basic Principles*, 4th ed. (Publishing House of Electronics Industry; McGraw-Hill Education, Xi'an, 2017), pp. 248–630.
[27]F. G. Della Corte, G. De Martino, F. Pezzimenti, G. Adinolfi, and G. Graditi, "Numerical simulation study of a low breakdown voltage 4H-SiC MOSFET for photovoltaic module-level applications," IEEE Trans. Electron Devices **65**(8), 3352–3360 (2018).
[28]F. Bouzid, F. Pezzimenti, and L. Dehimi, "Modelling and performance analysis of a GaN-based n/p junction betavoltaic cell," Nucl. Instrum. Methods Phys. Res., Sect. A **969**, 164103 (2020).
[29]N. Sanders and E. Kioupakis, "Phonon- and defect-limited electron and hole mobility of diamond and cubic boron nitride: A critical comparison," Appl. Phys. Lett. **119**, 062101 (2021).
[30]P. Scajev, V. Gudelis, A. Tallaire, J. Barjon, and K. Jarasiunas, "Injection and temperature dependent carrier recombination rate and diffusion length in free-standing CVD diamond," Phys. Status Solidi A **210**(10), 2016–2021 (2013).
[31]T. R. Alam, M. A. Pierson, and M. A. Prelas, "Design principles of narrow and wide bandgap-based betavoltaic batteries," IEEE Trans. Electron Devices **65**(12), 5518 (2018).